Supplementary Information

for

A self-healing Li-crosslinked elastomer promotes highly robust and conductive solid-electrolyte interphase

Zhijin Ju‡[ab], Xinyong Tao‡*[a], Yao Wang‡[a], Qing Yang‡[c], Tiefeng Liu[d], Jianwei Nai[a], Wenkui Zhang[a], Si Chen[a], Yujing Liu*[a], He Tian*[c] and Jun Lu*[d]

[a] College of Materials Science and Engineering, Zhejiang University of Technology, Hangzhou, 310014, China.

[b] College of Chemistry and Materials Engineering, Wenzhou University, Wenzhou, 325035, China.

[c] Center of Electron Microscope, School of Materials Science and Engineering, Zhejiang University, Hangzhou, 310027, China.

[d] College of Chemical and Biological Engineering, Zhejiang University, Hangzhou, 310027, China.

‡ These authors contributed equally to this work.

* Correspondence to: tao@zjut.edu.cn; yujingliu@zjut.edu.cn; hetian@zju.edu.cn; junzoelu@zju.edu.cn

Supplemental Figures

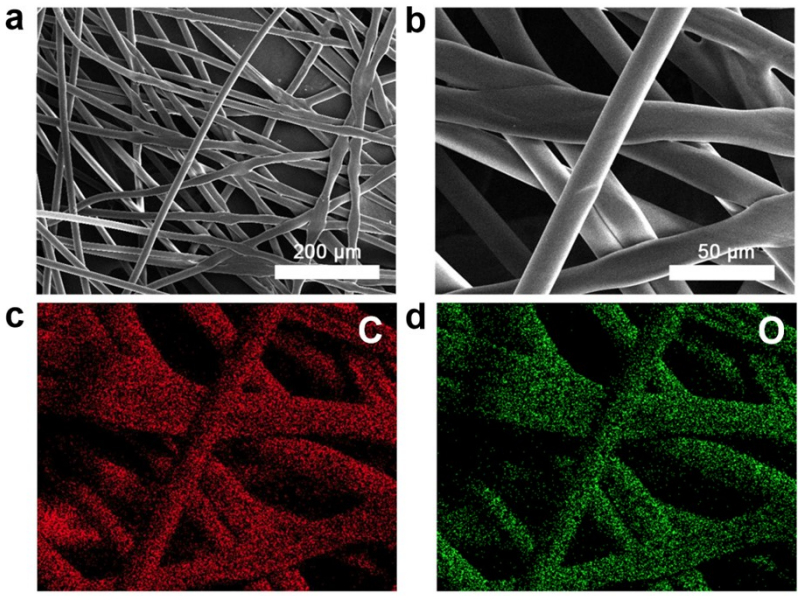

Fig. S1. Morphology characterization of PAP interlayer. a,b) SEM images of PAP. c,d) The corresponding elemental mappings. The PAP interlayer obtained through the melt-spinning process has a uniform fiber network structure. The elemental mappings indicate the uniform distribution of C and O within the PAP fibers.

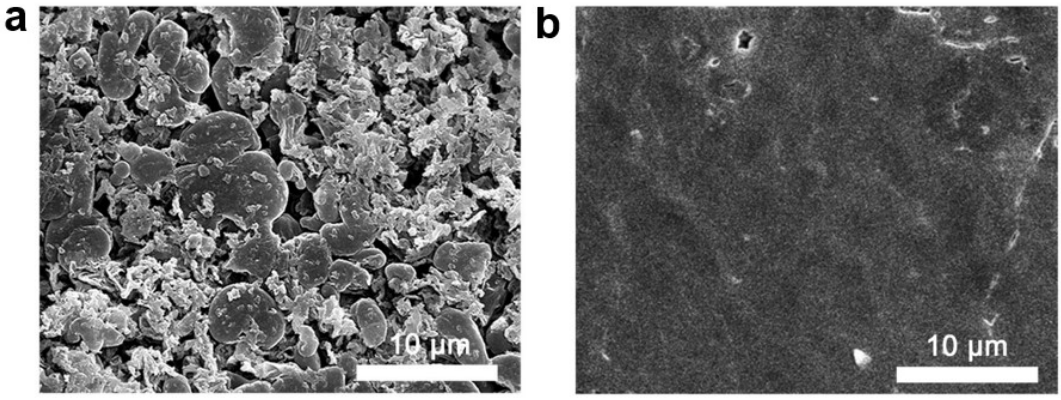

Fig. S2. Morphology characterization of the Li surface after cycling. a,b) SEM images of (a) bare Li and (b) PAP-covered Li after cycling. Compared with the dendritic morphology of bare Li, the surface of PAP-covered Li is dense and smooth after cycling.

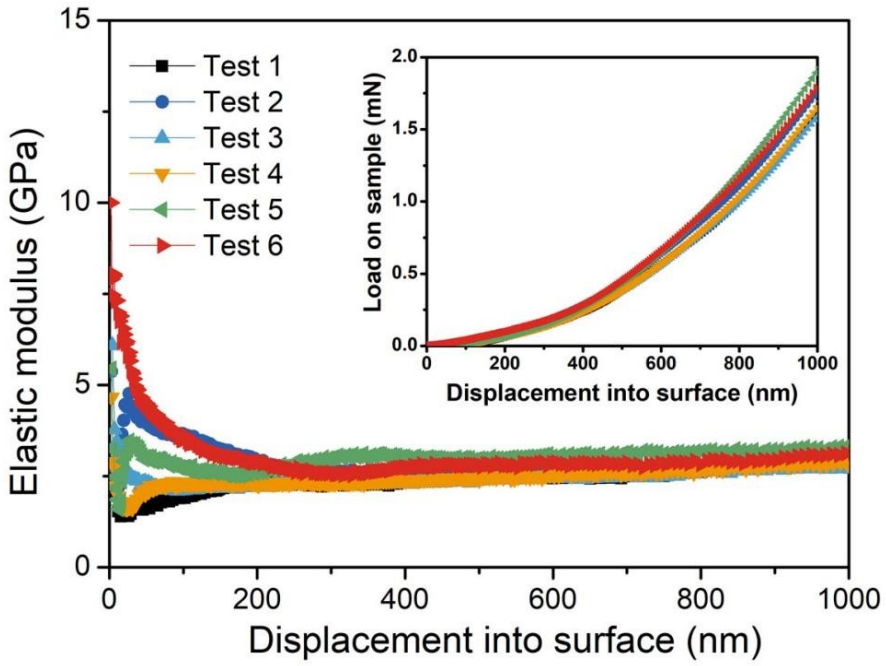

Fig. S3. Elastic modulus versus displacement curves of indentation test for ICE. Inset, corresponding load–displacement curves. Based on multiple nanoindentation measurements, the mean value of elastic modulus is ~2.8 GPa over a wide range of displacements.

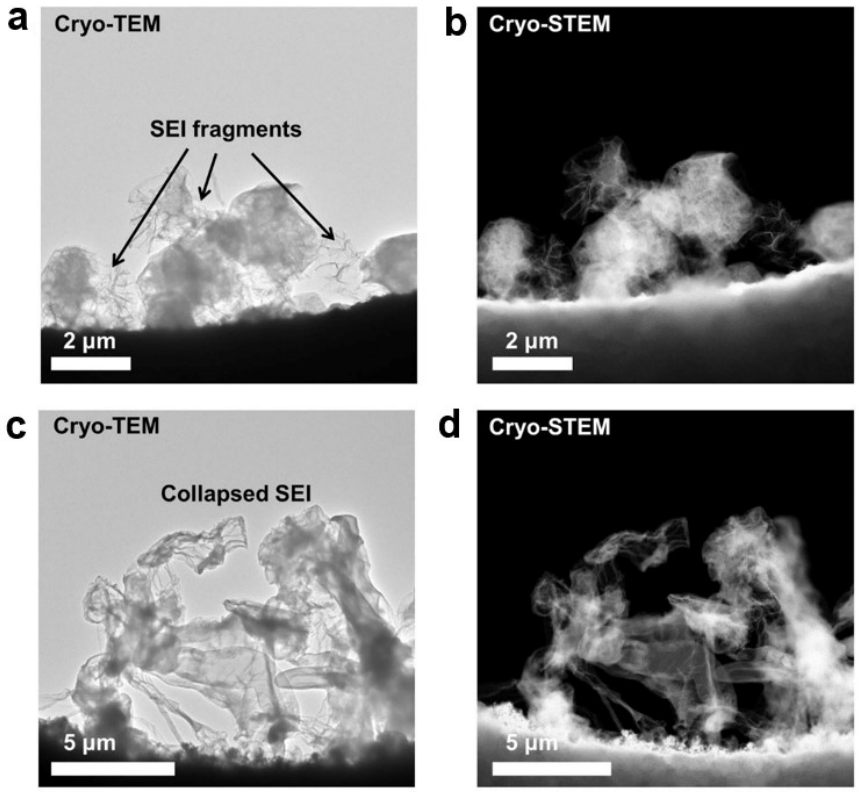

Fig. S4. Cryo-TEM and STEM images of the debris of the electrolyte-derived SEI after Li stripping with 0.2 mAh cm^{-2}. a-d) The SEI fragments of (a,b) Li spheres or (c,d) dendrites after Li stripping. It can be seen that the electrolyte-derived SEI structure of Li deposits is unstable and prone to collapse after Li stripping.

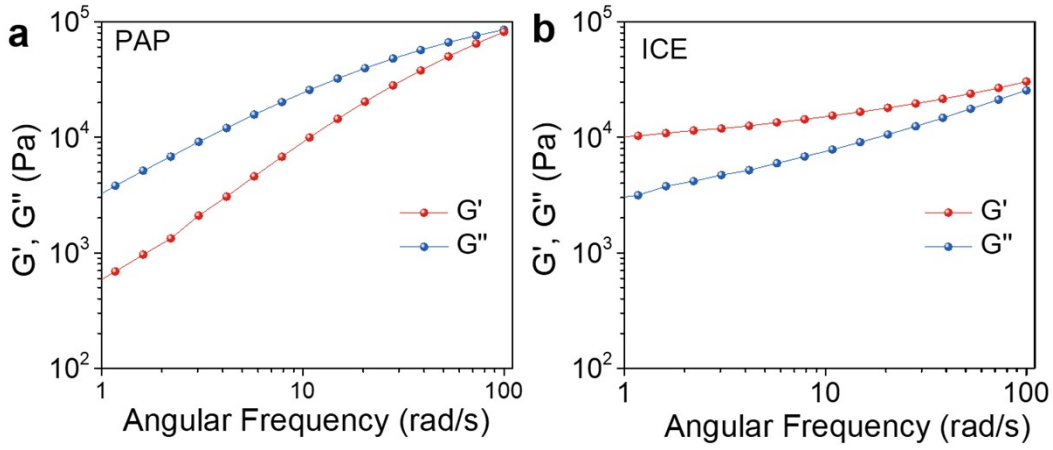

Fig. S5. Measurements of the dynamic moduli. a,b) The dynamic moduli (G' and G'') of neat PAP and ICE in the frequency range of 0.1 to 100 rad s^{-1}. It can be seen that the G'' of PAP is always higher than its G', while the G'' of ICE starts to be lower its G' after the lithiation reaction.

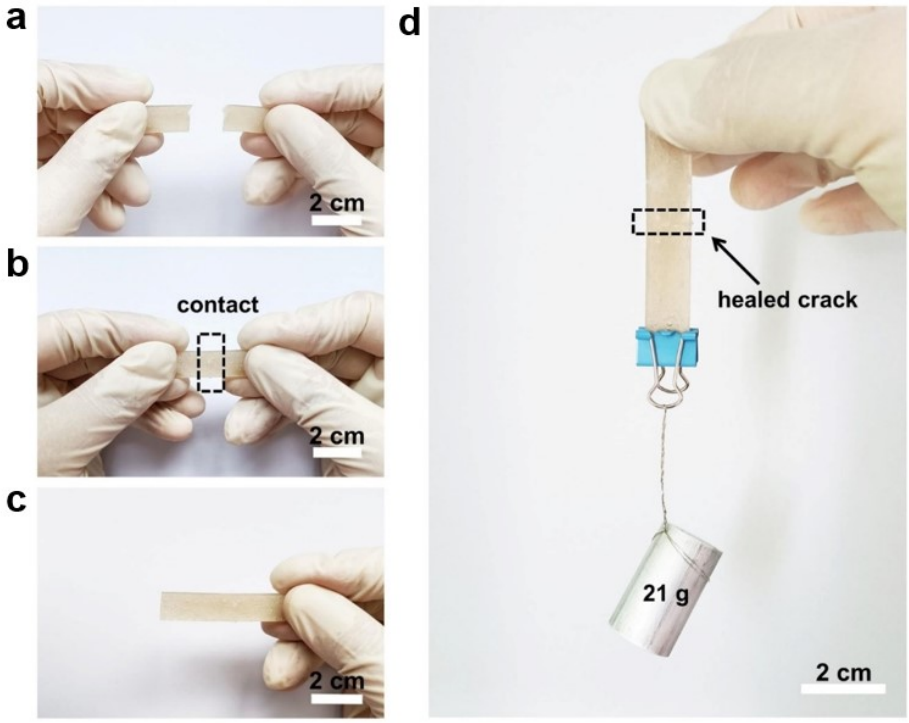

Fig. S6. Photographs showing the self-healing feature of the ICE. a) The sample of ICE cut off in the middle. b) Two fractured parts of ICE were closely contacted and the joint interface was fumigated by DOL solvent. c) The ICE was healed spontaneously after only 10 s. d) The healed ICE was stretched with 21 g weights, intuitively suggesting that the ICE possesses self-healing properties during the battery cycling.

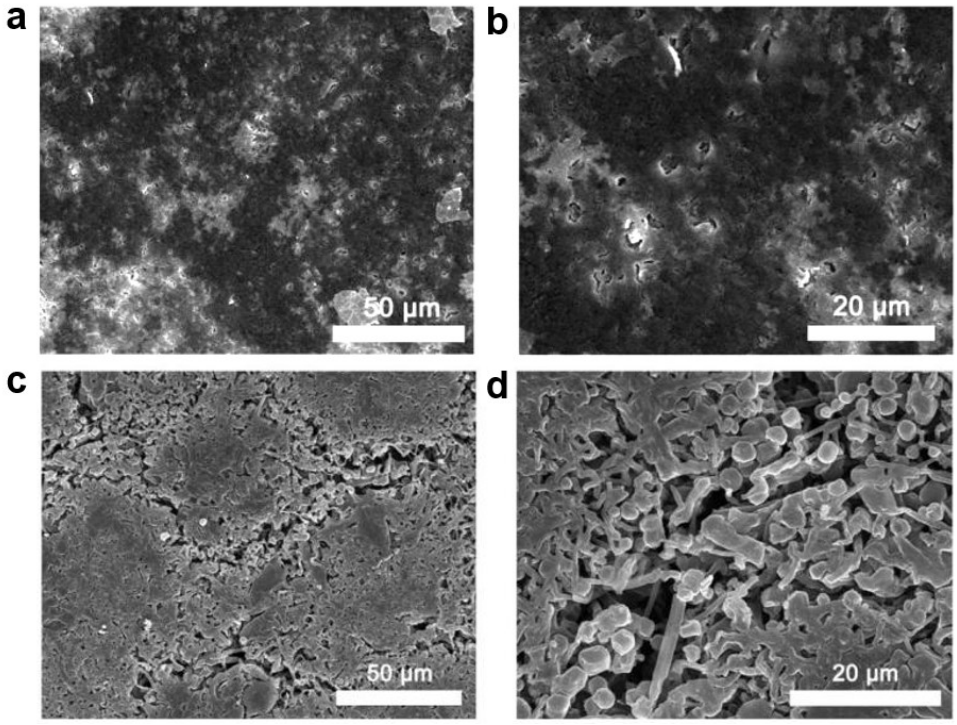

Fig. S7. Morphologies of the Li surface after cycling. a,b) SEM images of Li anode with the ICE-SEI film after 4000 cycles at 3 mA cm^{-2} with a cycling capacity of 1 mAh cm^{-2}. c,d) SEM images of bare Li anode after 1000 cycles at 3 mA cm^{-2} with a cycling capacity of 1 mAh cm^{-2}. After long-term cycling, the surface of ICE-SEI@Li anode presents smooth morphology, while the surface of bare Li anode is porous with a dendritic structure.

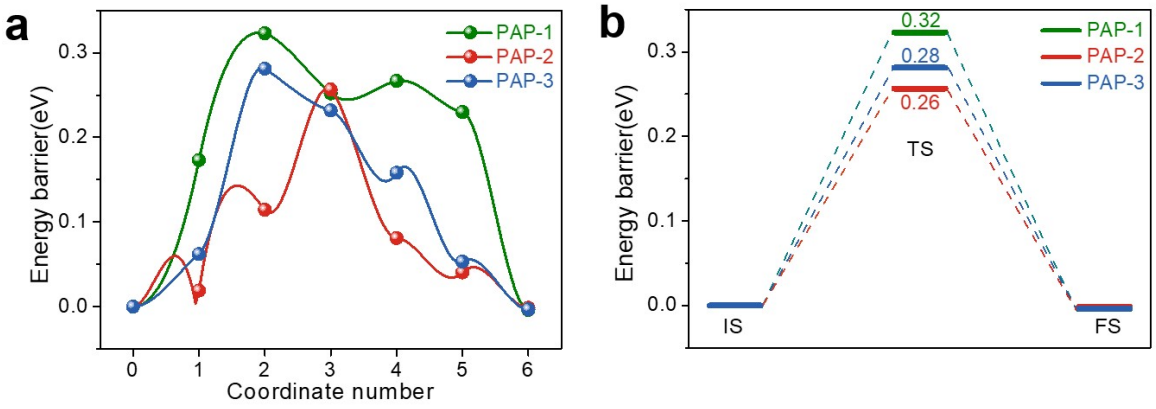

Fig. S8. Calculations for Li diffusion on PAP chains after lithiation. a,b) The minimum energy path for (a) Li diffusion and (b) the corresponding values of energy barrier on the PAP chain with the different number of absorbed Li atoms. It reveals the energy barrier of Li atom diffusion on the PAP chain reduces when the number of absorbed Li atoms increases.

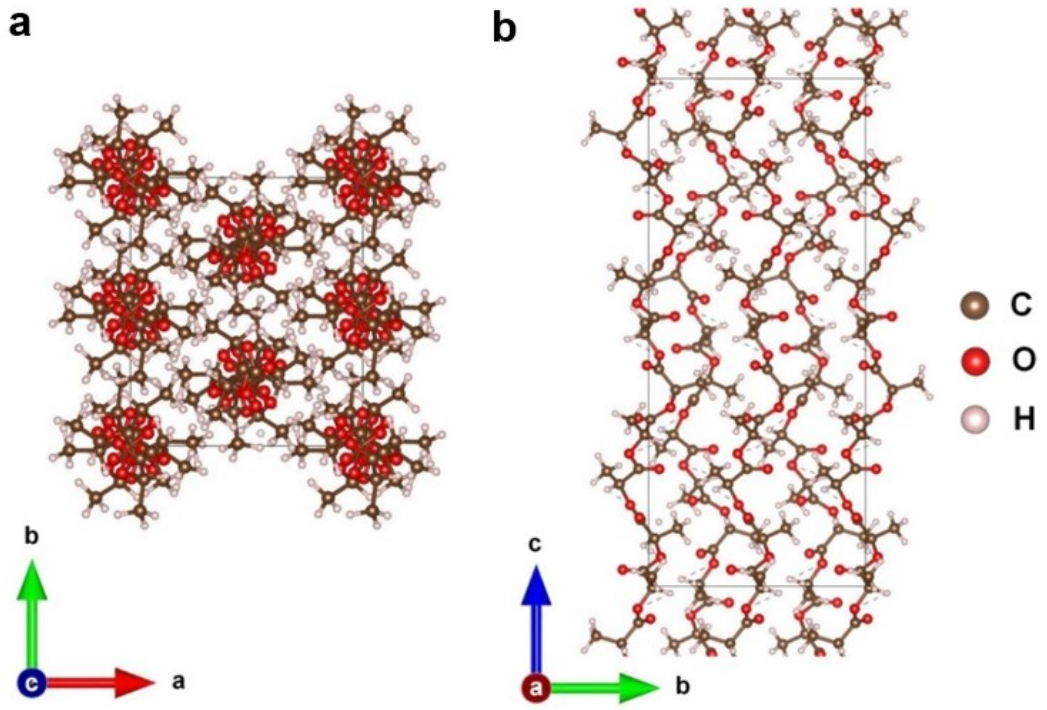

Fig. S9. The molecular structure of PAP. a,b) The molecular structure of PAP viewed from the (a) top view and (b) elevation view. The presented space group of PAP is $P2_12_12_1$ and its unit cell contains two helices which were arranged in an antiparallel symmetry.[1]

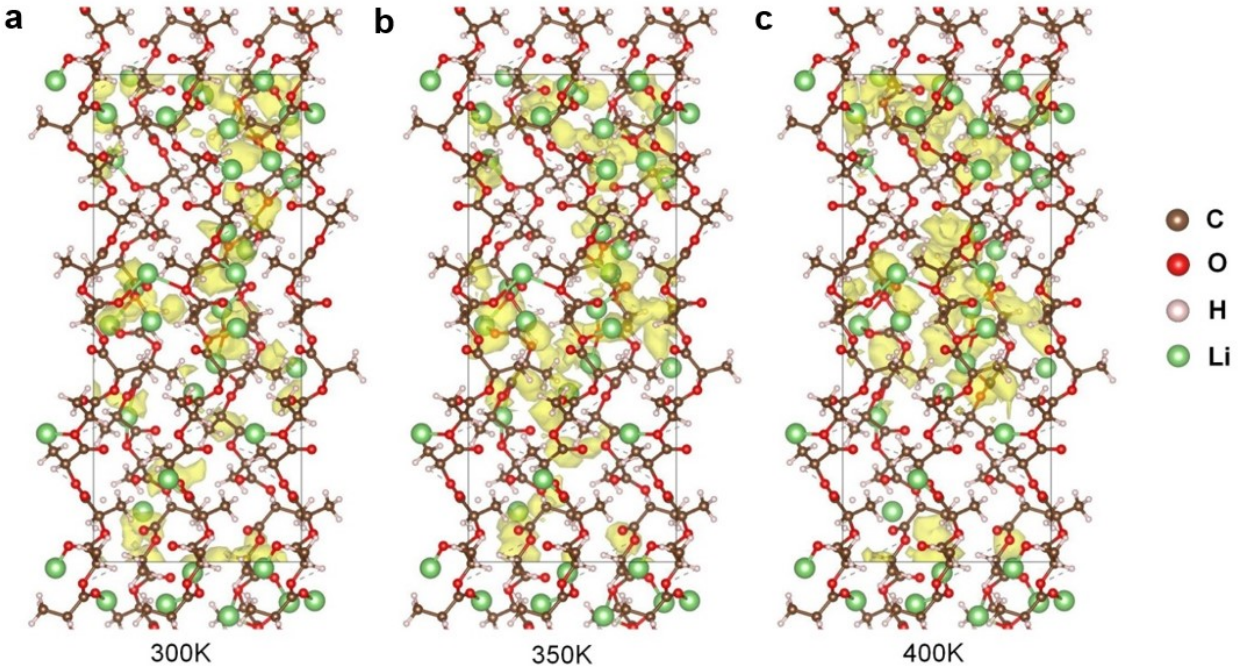

Fig. S10. Li-ion probability densities in ICE at different temperatures. a-c) The molecular dynamics study of ICE at (a) 300 K, (b) 350 K, and (c) 400 K. Isosurfaces indicate the probability densities of Li ions. It shows that the migration is relatively local at 300 K, relatively delocalization at 350 K, and the decomposition of PAP occurs at 400 K.

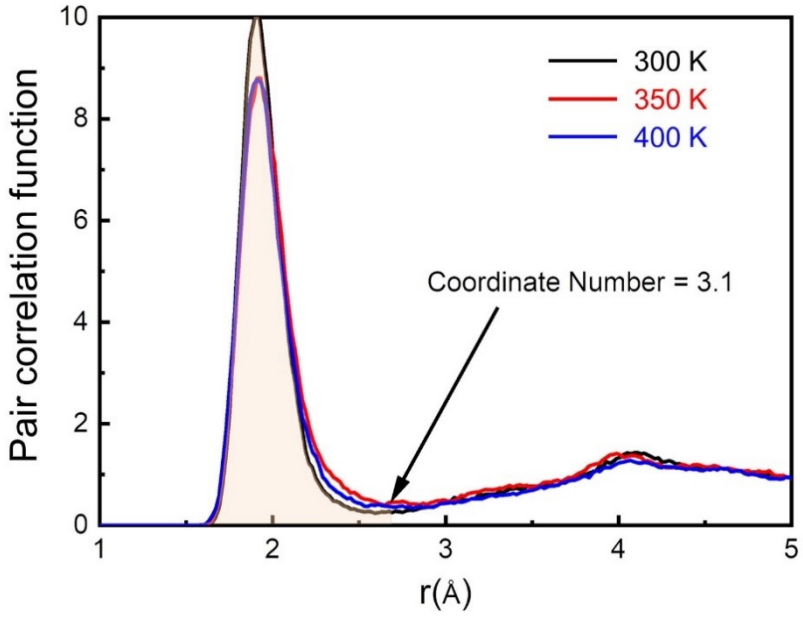

Fig. S11. The partial radial distribution function of Li-O at different temperatures. By integrating gr for the first trough of 300 K, it can be calculated that the coordination number of O atoms around the Li atom is 3.1, meaning one Li atom will coordinate with three O atoms.

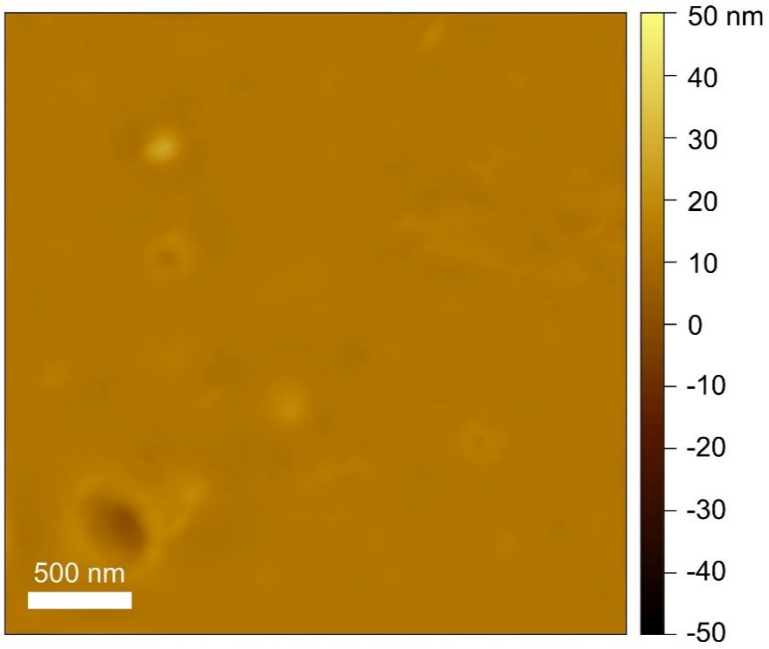

Fig. S12. The measured topography of ICE based on AFM-IR characterization. The AFM image depicts a relatively flat surface with small height differences.

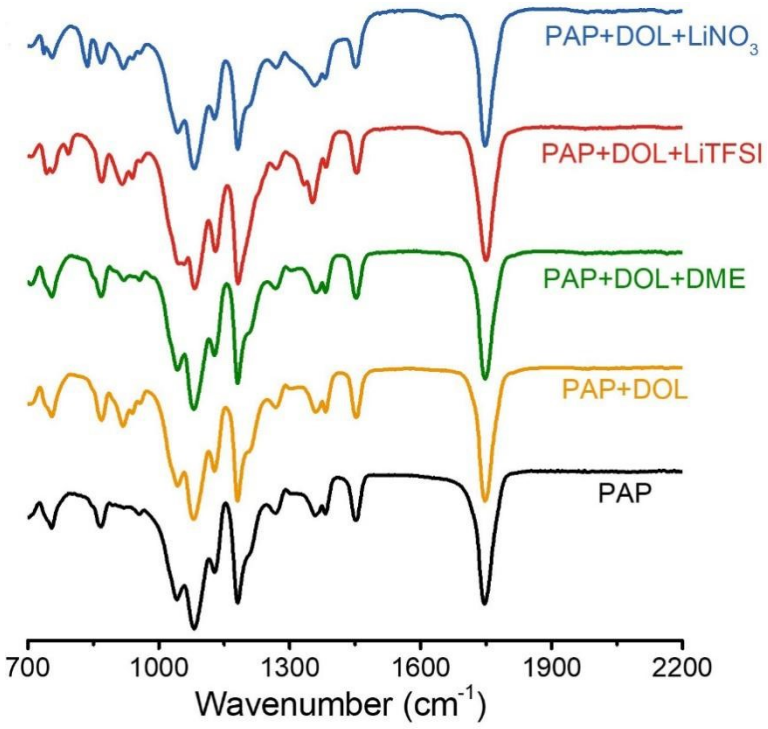

Fig. S13. The FTIR spectra of PAP containing various chemical compositions. It can be seen that the peak at ~920 cm^{-1} belongs to the DOL solvent after the introduction of DOL into PAP. Besides, some peaks at ~794 and ~1330 cm^{-1} are assigned to the LiTFSI, and a peak at 836 cm^{-1} is ascribed to the $LiNO_3$.

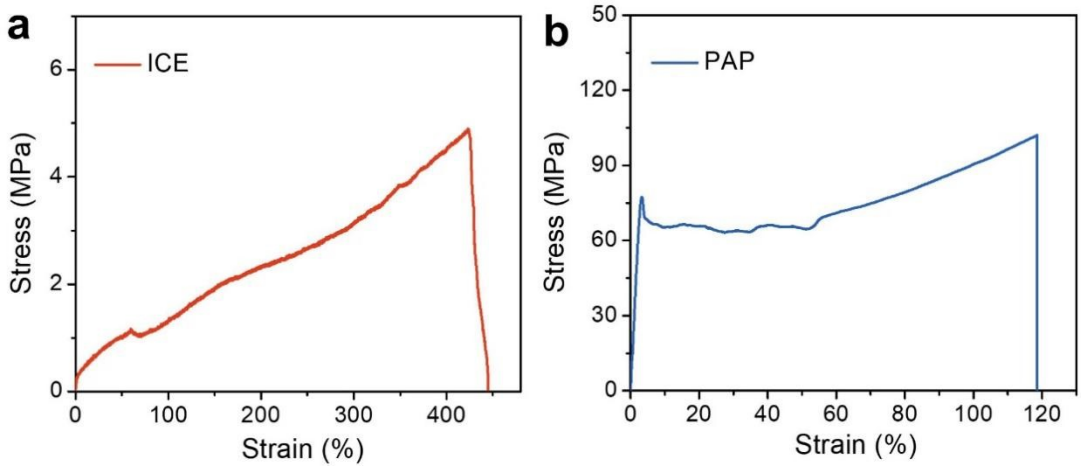

Fig. S14. The stress−strain curves of ICE and PAP. a,b) The stress−strain curves are shown for ICE and PAP. To investigate the mechanical properties of the ICE, we measured its tensile modulus based on strain−stress curves. The tensile strength of ICE is 4.9 MPa and can afford a tensile strain of ~445% before fracture. However, the tensile strength of compact PAP film is 102 MPa with a lower breaking elongation of ~118%.

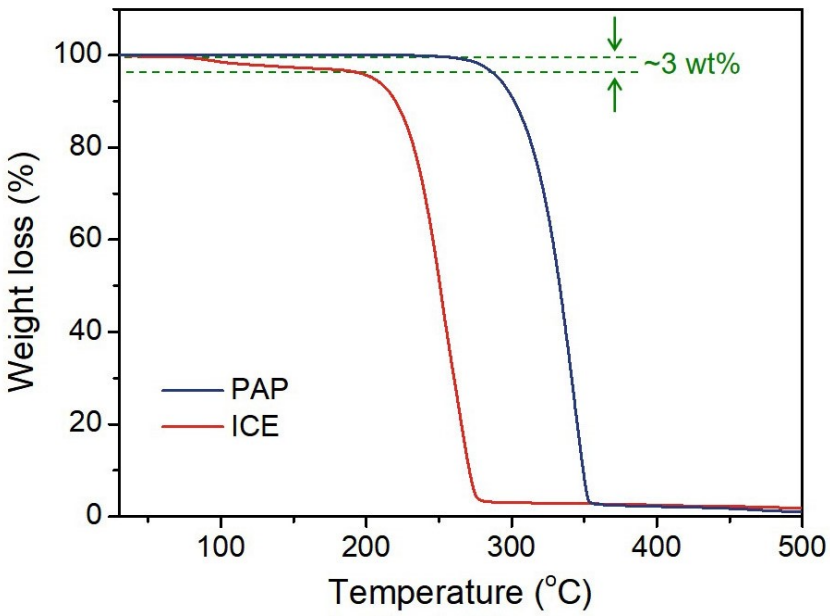

Fig. S15. The TGA curves of PAP and ICE. Compared with the TG curve of PAP, there is ~3 wt% weight loss for ICE from 50 to 200 °C, which mainly accounts for the dissipation of combined solvent.

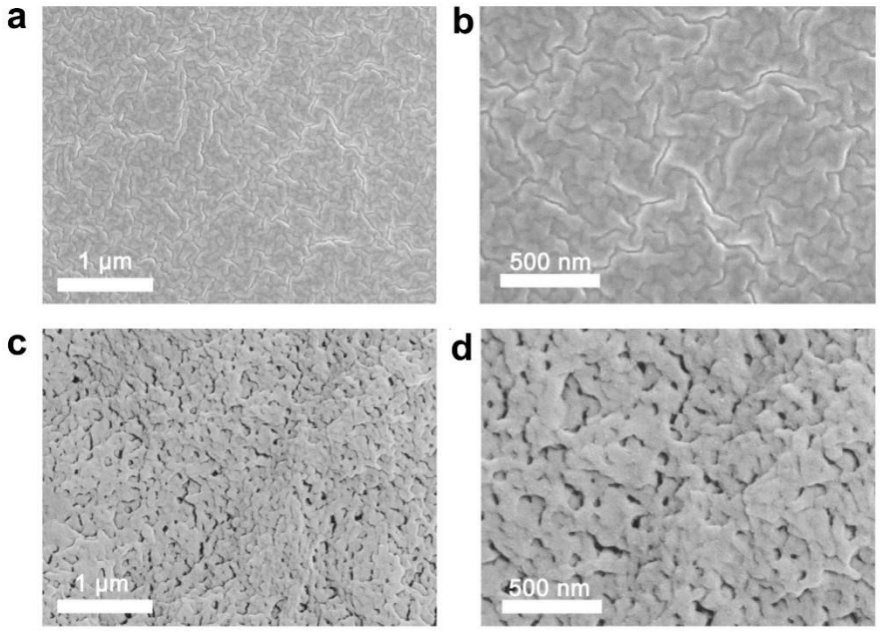

Fig. S16. Morphologies of ICE. a-d) SEM images of ICE (a,b) before and (c,d) after freeze drying. Due to solvent volatilization after freeze drying, many gaps appear in the dense structure of ICE.

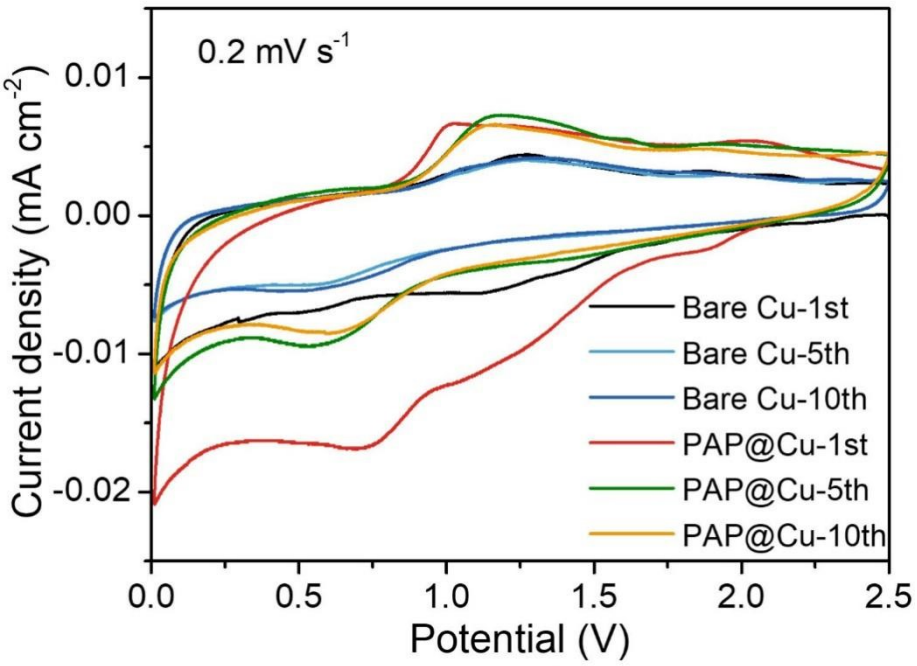

Fig. S17. Cyclic voltammetry of half cells with PAP@Cu and bare Cu at 0.2 mV s^{-1}. It shows that there appear new peaks at ~1.88 V and ~0.75 V in the first cycle for the PAP@Cu electrode, suggesting the electrochemical reduction of PAP on the Cu electrode during cycling.

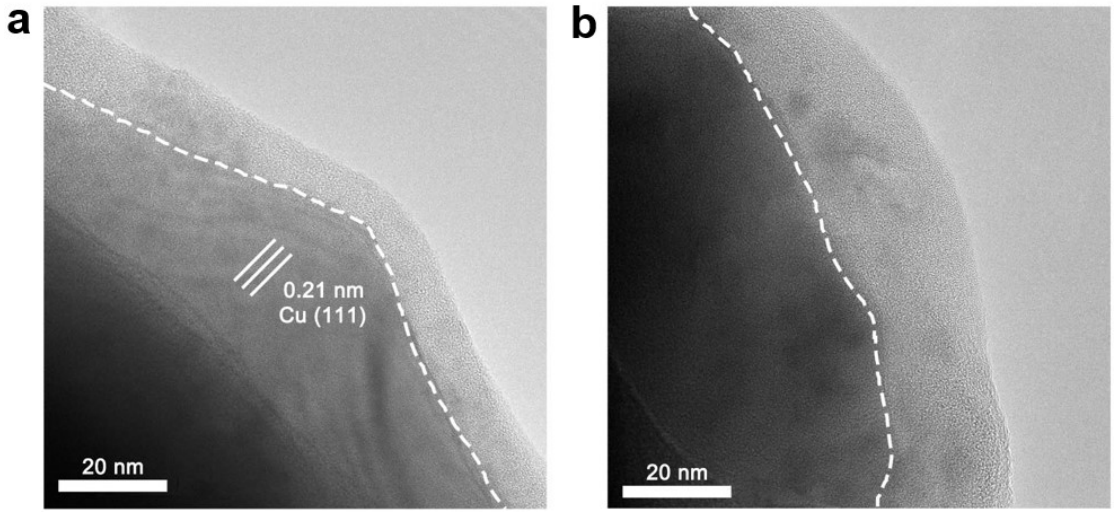

Fig. S18. Morphologies of SEI on Cu grid. a,b) Comparisons of SEI morphology derived from (a) electrolytes and (b) PAP interlayer after discharging to 0.01 V. It shows that the PAP-derived SEI is thicker than that of electrolyte-derived SEI, meaning that PAP will participate in the formation of SEI layer after cycling.

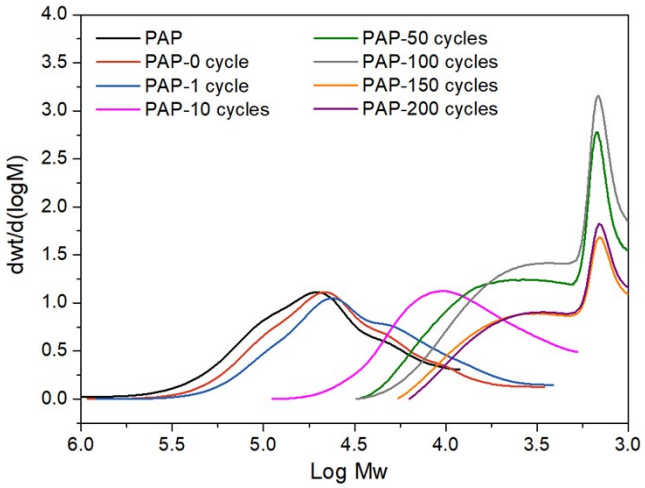

Figure S19. GPC traces of the PAP after various cycles. The decomposition of pristine PAP upon cycling typically involves a gradual decrease in molecular weight and stabilizes at certain values.

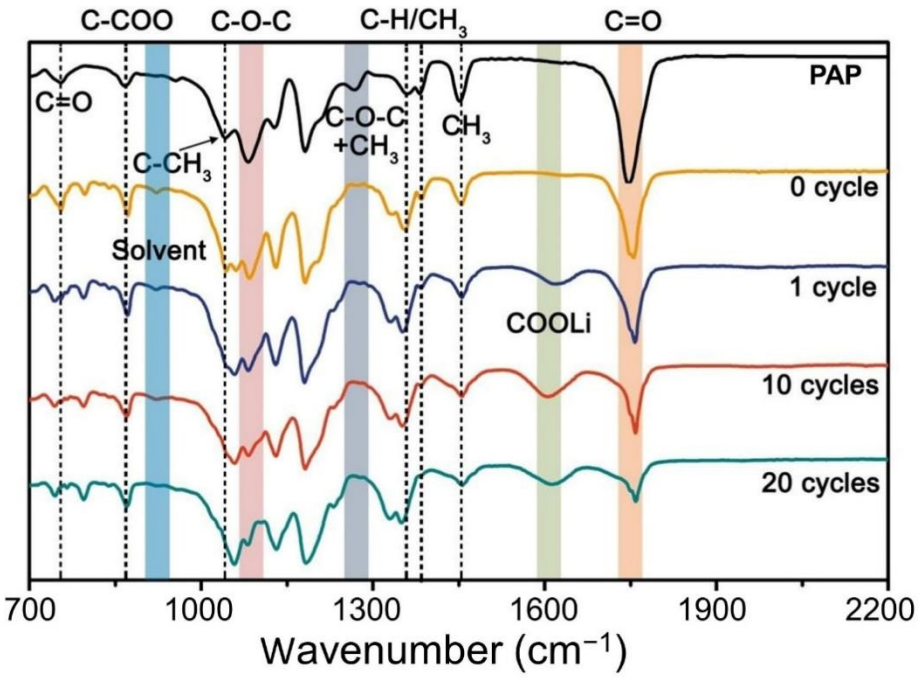

Fig. S20. *Ex-situ* FTIR spectra of the pristine PAP and ICE after different cycles. For the pristine PAP interlayer, the peaks centered at 1083 cm^{-1} correspond to C−O−C symmetric stretching mode and their intensities gradually decrease in further electrochemical cycles. Both the $-CH_3$ asymmetric deformation (at 1456 cm^{-1}) and C=O vibration (at 756 and 1748 cm^{-1}) also have an obvious decrease in intensity with cycling. Meanwhile, the peaks at 1269 cm^{-1} assigned to C−O−C stretching and C−H deformation coupling mode almost disappear. The peaks of C-CH_3 at 1043 cm^{-1} show a blueshift after lithiation. Besides, there is a new broad peak at 1620 cm^{-1}, which can be ascribed to the $-COO^-$ asymmetric vibration mode.[2,3] Some peaks (at 794 and 1330 cm^{-1}) belonging to the Li salts in electrolytes also can be found (Fig. S13).

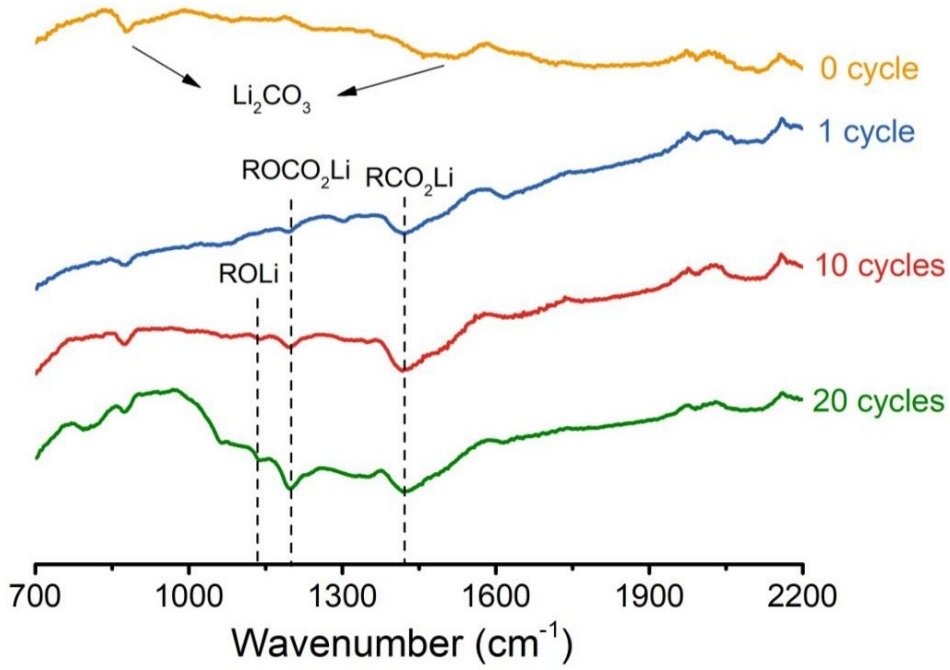

Fig. S21. The *ex-situ* FTIR spectra of the electrolyte-derived SEI after different cycles. It can be seen that the pristine SEI on bare Li mainly consists of Li_2CO_3. Upon cycling, there are lots of organic components (including ROLi, $ROCO_2Li$, and RCO_2Li) for the SEI derived from electrolyte decomposition.[4]

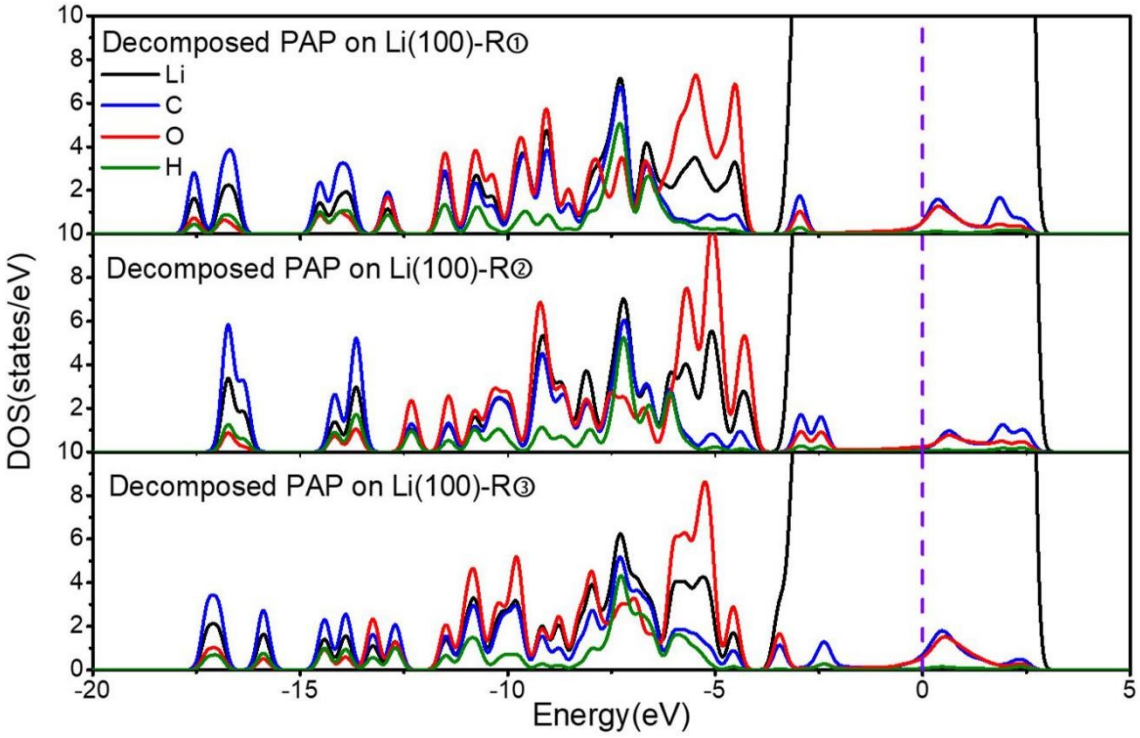

Fig. S22. The PDOS plots of the decomposed PAP. The PDOS plots show that the LUMO-HOMU gap in route 1 is slightly larger than that in route 2, which indicates that PAP decomposed process in route 2 needs to gain more electrons from the Li metal surface than that in route 1. The analysis of PDOS results reveals that PAP polymer maintains insulating property after C−O dissociation and reaction route 1 is more favorable than other routes since the prerequisite of less electron number injection.

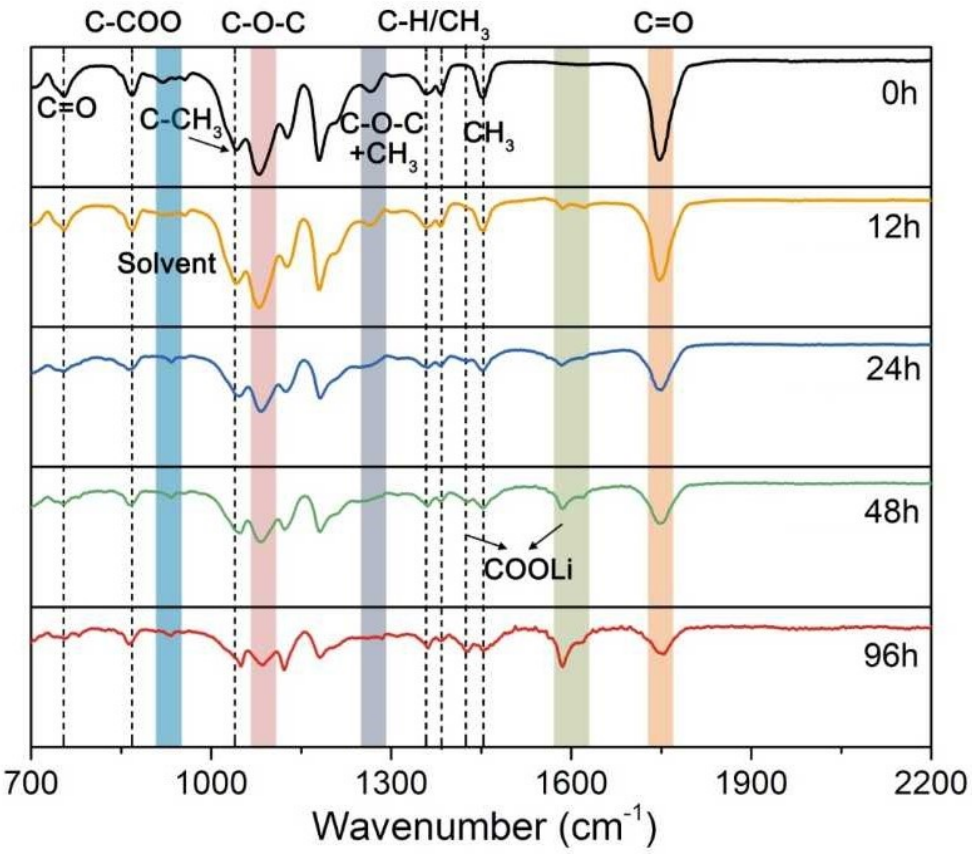

Fig. S23. The FTIR spectra of PAP after different lithiation times. With the prolongation of lithiation time, the intensity of peaks ascribed to –COOLi groups gradually increases, suggesting a more complete decomposition of PAP into ICE.

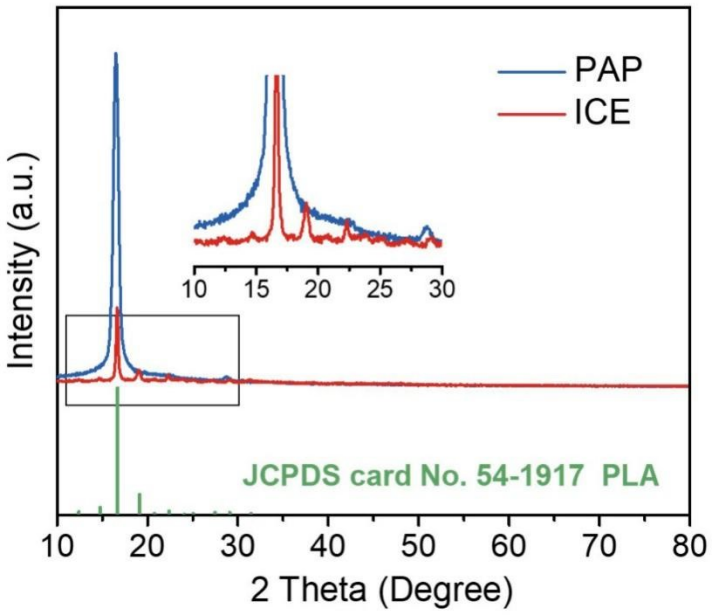

Fig. S24. The XRD patterns of PAP and ICE. It can be found that the intensity of peaks is decreased after the lithiation reaction of PAP, further declaring the decomposition of PAP into ICE.

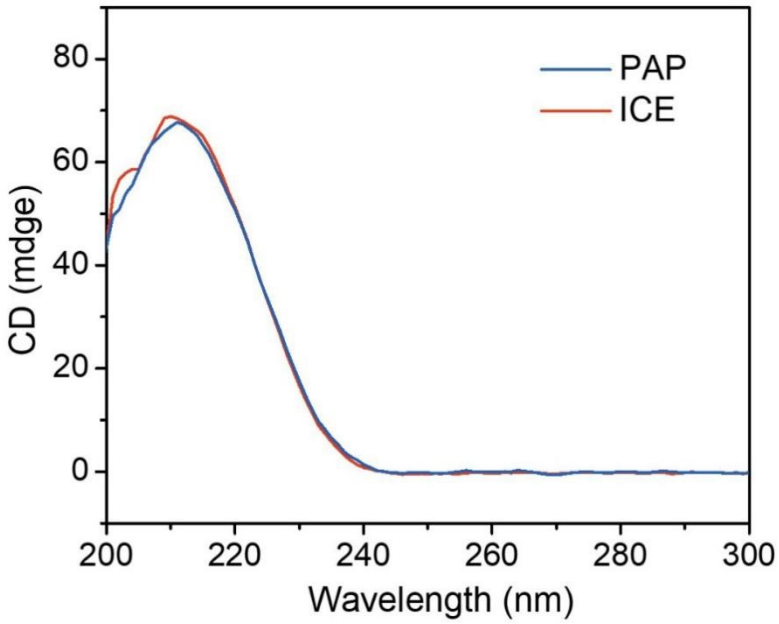

Fig. S25. The circular dichroism (CD) spectra of PAP and ICE. It indicates that both the PAP and ICE possess a positive dichroic band at around 210 nm, ascribed to the n→π* absorption of the ester group.[5]

a

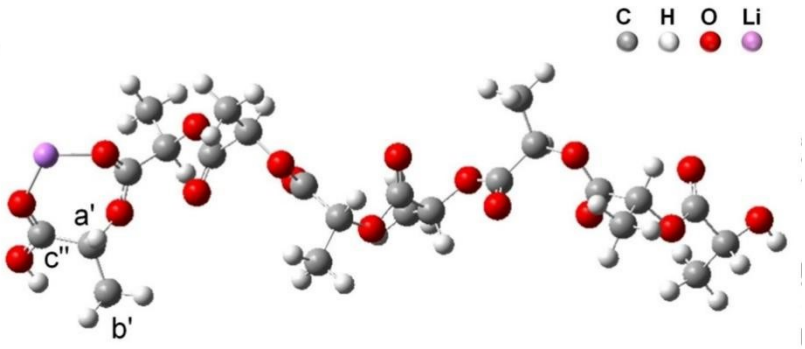

b

Chemical shift	a'	b'	c''
^{1}H	4.99	1.81	/
^{13}C	81.14	16.83	181.77

Fig. S26. The calculated chemical shifts. a) The ICE molecule used in the calculation of NMR chemical shift parameters. b) Calculation results of the chemical shift of carbon and hydrogen when Li ion interacts with the ester groups of PAP. Due to the strong interaction of Li ions with the ester groups, the peak of ^{13}C shifts from 170 ppm to 181.77 ppm, thus leading to the newly formed peak of c''.

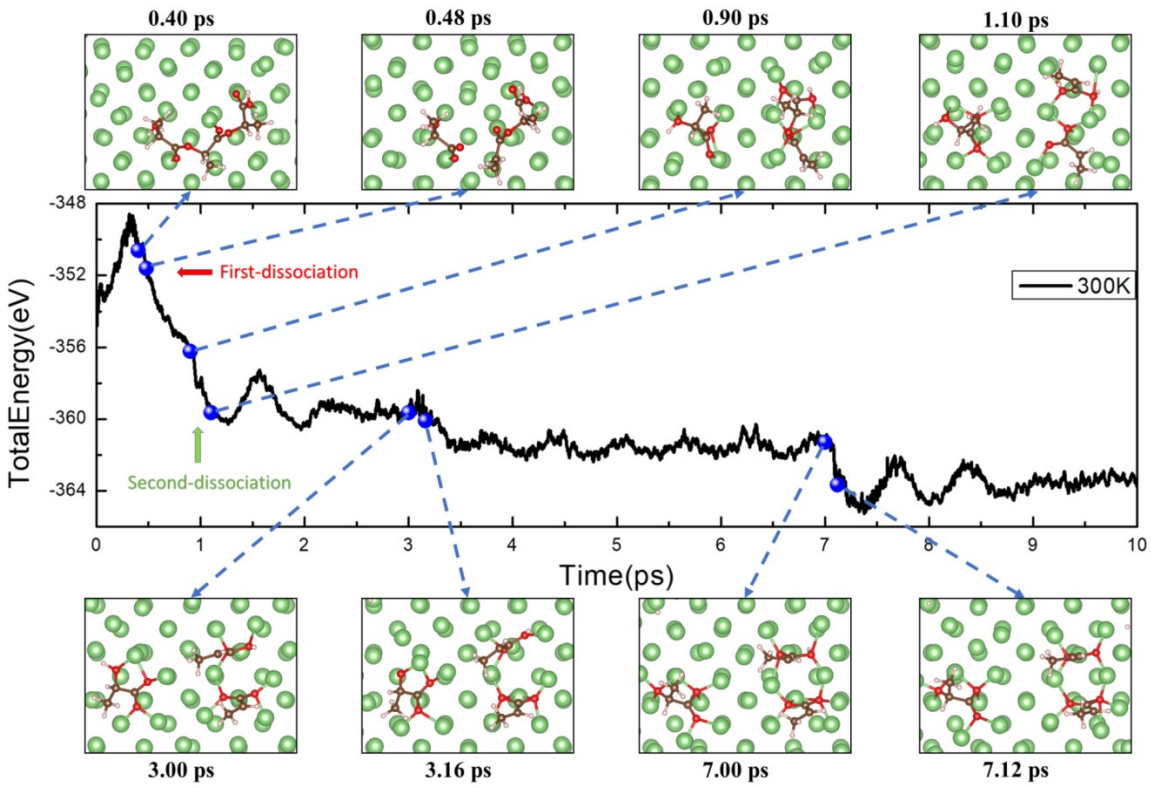

Fig. S27. The molecular dynamics simulation of PAP on the Li slab at different times. It shows that the C–O bonds will break to form the –COOLi groups with the relaxation time, in good agreement with the experiment results.

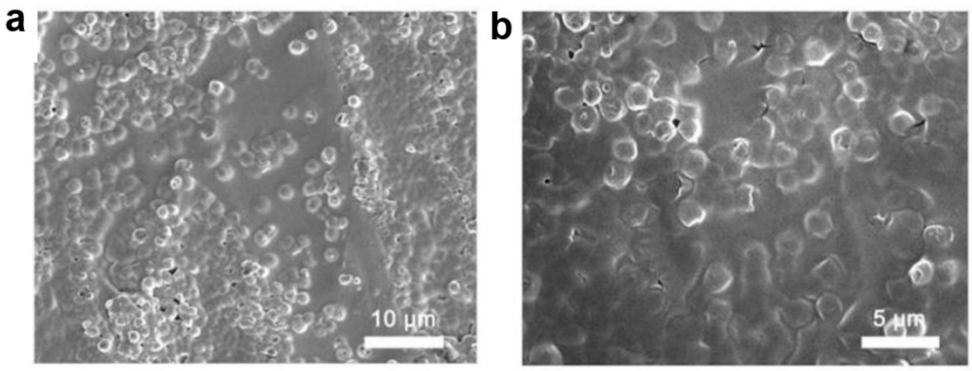

Fig. S28. Morphology of the Li deposited with ICE film. a,b) SEM image of Li deposits in the presence of (a) ICE film and (b) the magnified SEM image formed on Cu foil at 2 mA cm^{-2} with a fixed capacity of 1 mAh cm^{-2}. It can be seen that the Li deposits will be coated with a polymer layer in the presence of ICE, declaring that the generated ICE will participate in the SEI formation during cycling.

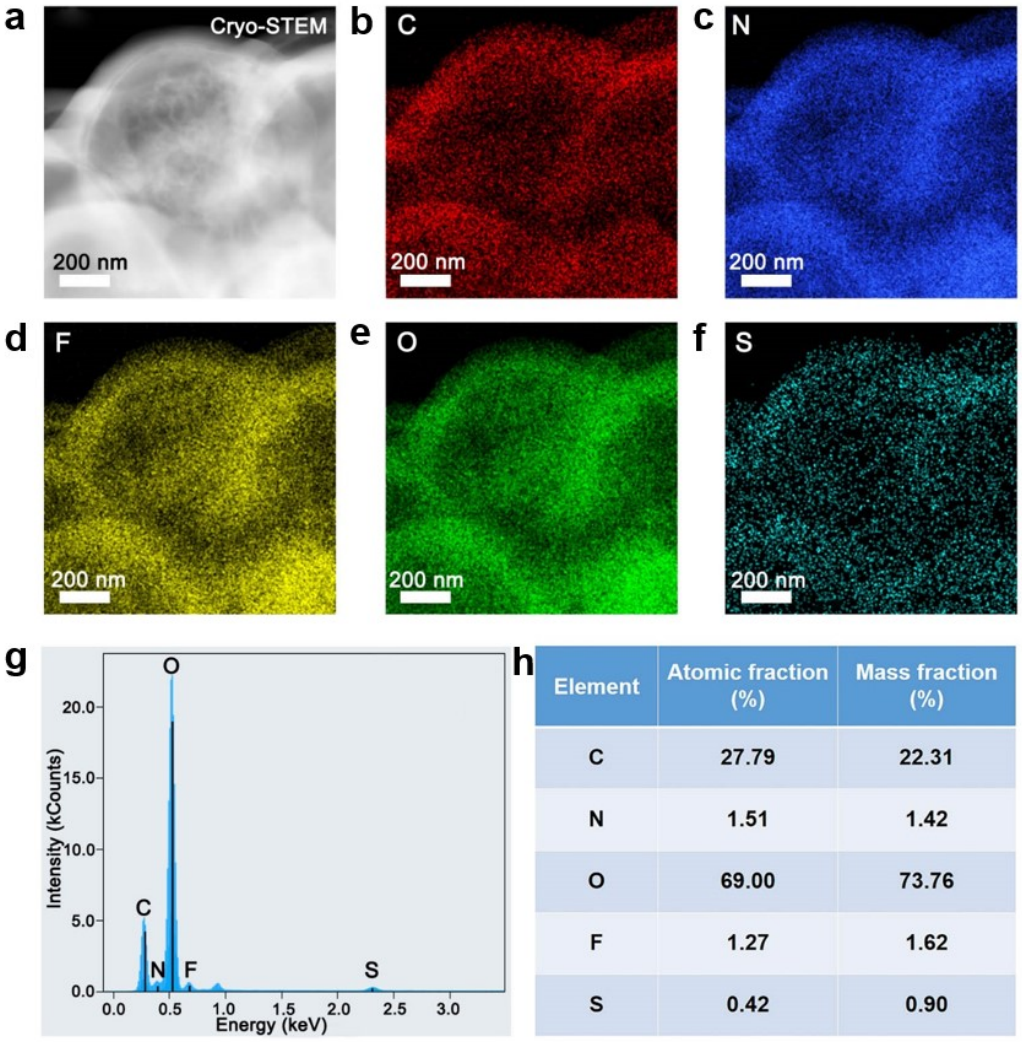

Element	Atomic fraction (%)	Mass fraction (%)
C	27.79	22.31
N	1.51	1.42
O	69.00	73.76
F	1.27	1.62
S	0.42	0.90

Fig. S29. Morphologies and elemental analysis of SEI and plated Li on Cu grid in the presence of ICE. a) Cryo-STEM image of the Li deposits with the SEI containing ICE. b-f) The corresponding elemental mapping images in (a). g) The spectrum of element intensity. h) The relevant atomic and mass fraction of varied elements. Due to the incorporation of ICE, Li deposits with the SEI containing ICE contain a high fraction of C.

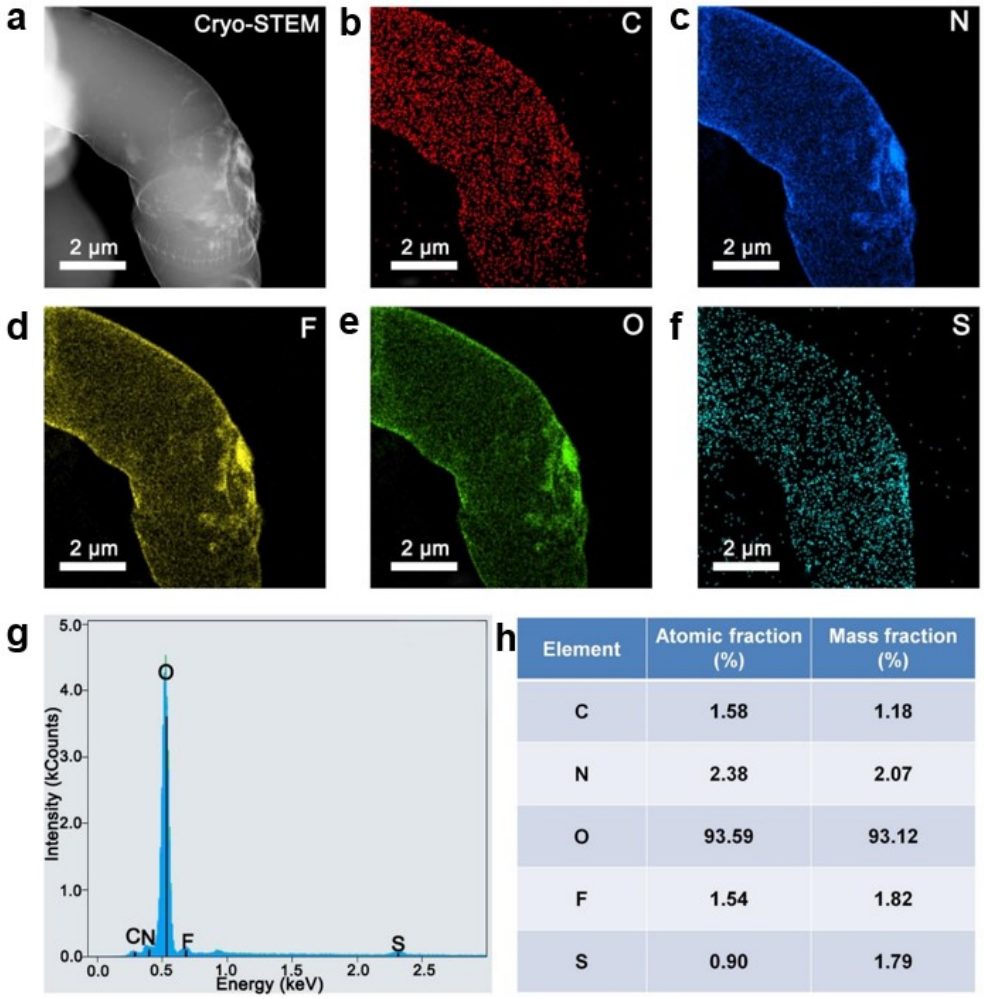

Element	Atomic fraction (%)	Mass fraction (%)
C	1.58	1.18
N	2.38	2.07
O	93.59	93.12
F	1.54	1.82
S	0.90	1.79

Fig. S30. Morphologies and elemental analysis of SEI and plated Li on Cu grid. a) Cryo-STEM image of the bare Li deposits. b-f) The corresponding elemental mapping images in (a). g) The spectrum of element intensity. h) The relevant atomic and mass fraction of varied elements. A high fraction of O within bare Li deposits is mainly because of the high concentrations of inorganic and organic components derived from electrolyte decomposition.

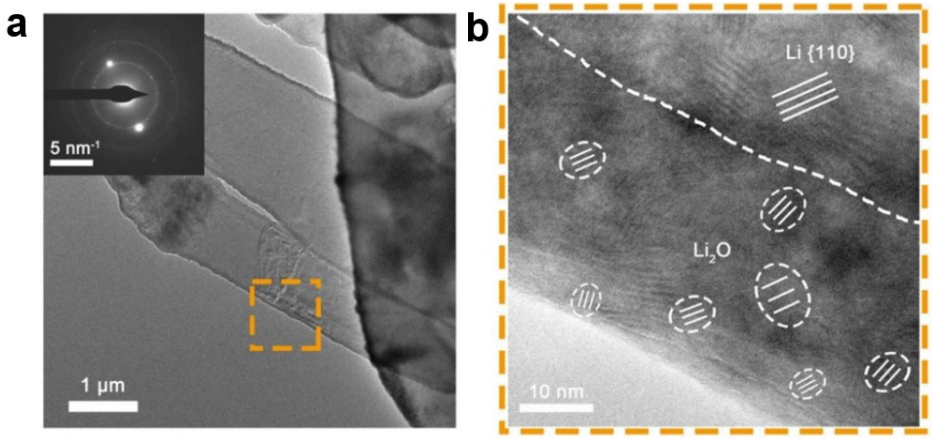

Fig. S31. Microstructures and components of electrolyte-derived SEI. Low-magnification (a) and HRTEM (b) images of Li dendrites formed without PAP. It shows that Li metal tends to grow into dendritic morphology without PAP and its SEI possesses a typical mosaic model.

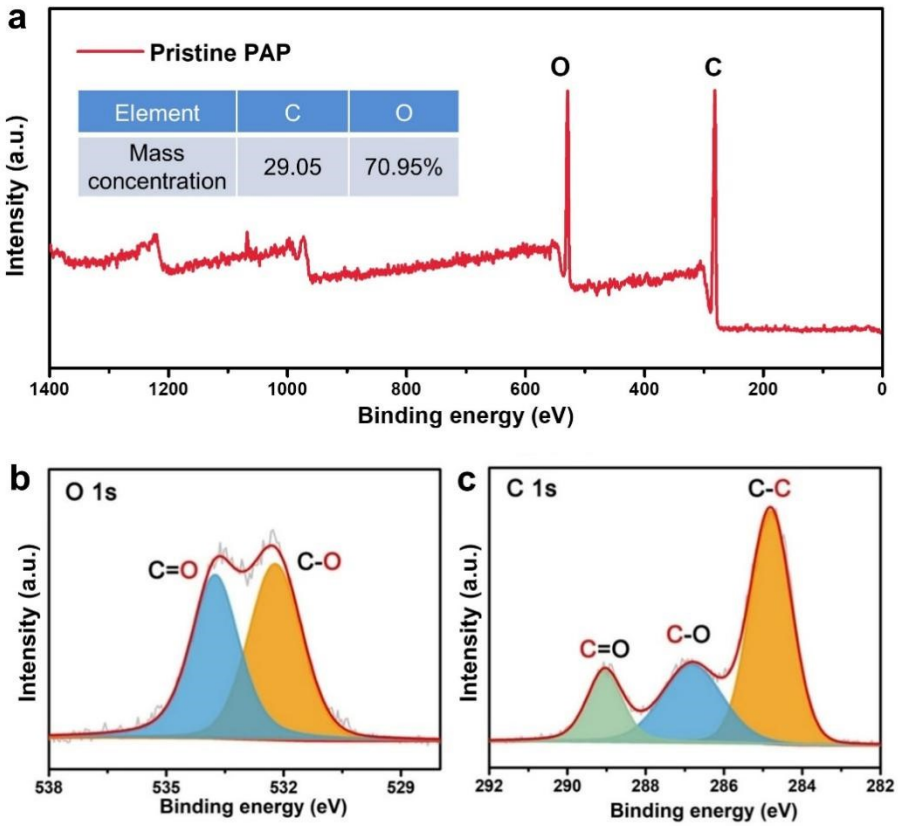

Fig. S32. XPS results of the pristine PAP. a) XPS characterizations of PAP. b,c) High-resolution (b) O 1s and (c) C 1s spectra in XPS. The high-resolution XPS spectra show that the molecular structure of PAP mainly includes C−C, C−O, and C=O bonds.

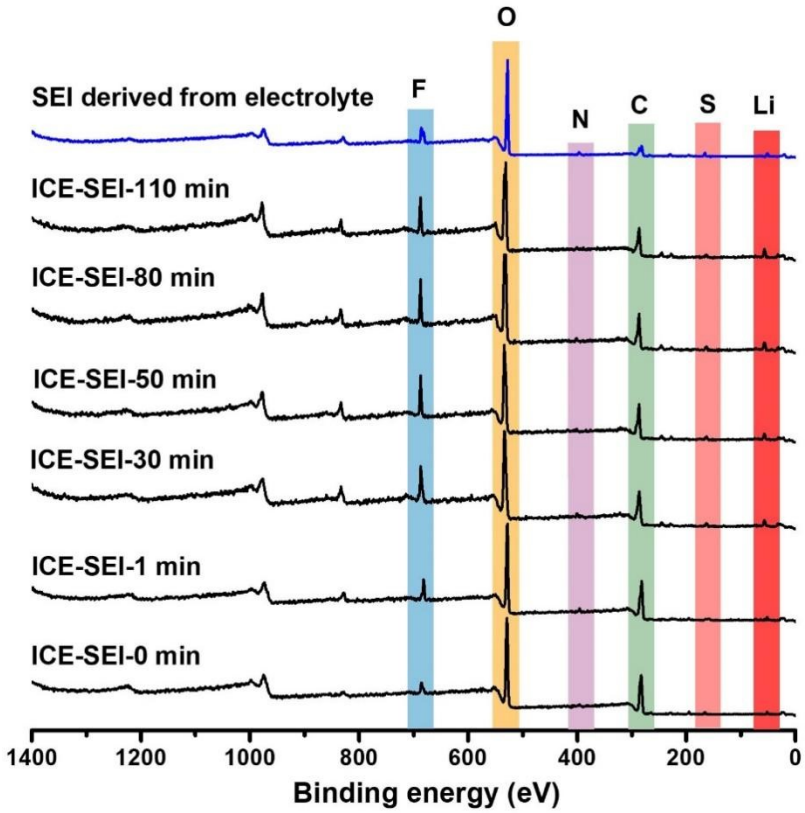

Fig. S33. XPS elemental concentration analysis of the ICE-SEI and electrolyte-derived SEI. Owing to the incorporation of ICE during cycling, the ICE-SEI contains a high concentration of C compared to the SEI derived from electrolyte.

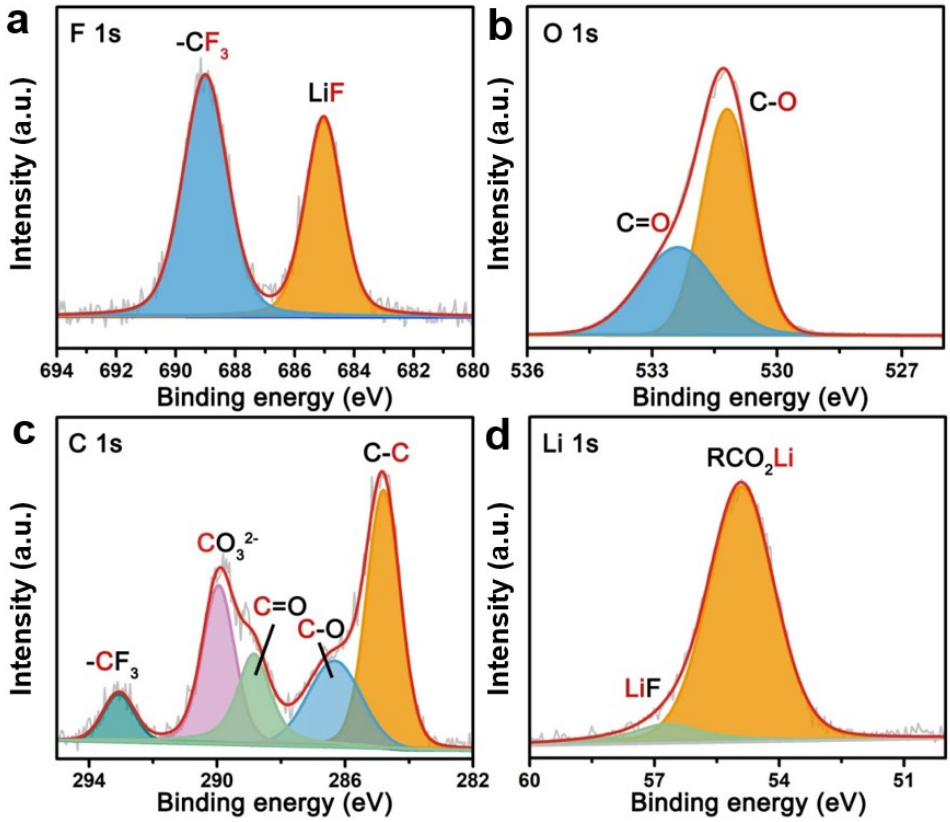

Fig. S34. XPS spectra of electrolyte-derived SEI. a-d) High-resolution XPS (a) F 1s, (b) O 1s, (c) C 1s, and (d) Li 1s spectra of the SEI derived from electrolyte. The SEI derived from electrolyte is mainly composed of organic and inorganic species stemming from the decomposition of the solvent and Li salts.

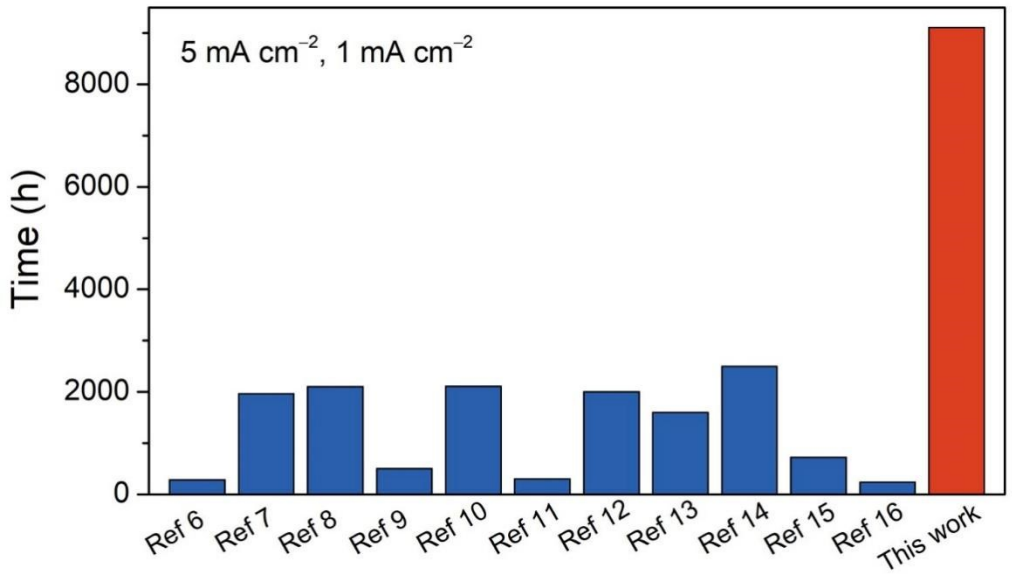

Fig. S35. Comparison of the lifespan of symmetric cells with ICE-SEI@Li and that of previously-reported Li metal anode stabilization strategies. It includes PPy-filled MOF host[6], PVA-In_2S_3 coating[7], GO-g-PAM@PP separator[8], lithiophilic vertical cactus-like framework[9] xonotlite nanowires separator[10], UiO-66-ClO_4/Li-Nafion film[11], $MnCO_3$/PP/$MnCO_3$ separator[12], V_2O_5-Ni foam host[13], LiPON@PP separator[14], CF-Mg_3N_2 collector[15], or $LiBF_4$-$LiNO_3$ additives[16]. All symmetric cells were cycled at 5 mA cm^{-2} with a capacity of 1 mAh cm^{-2}.

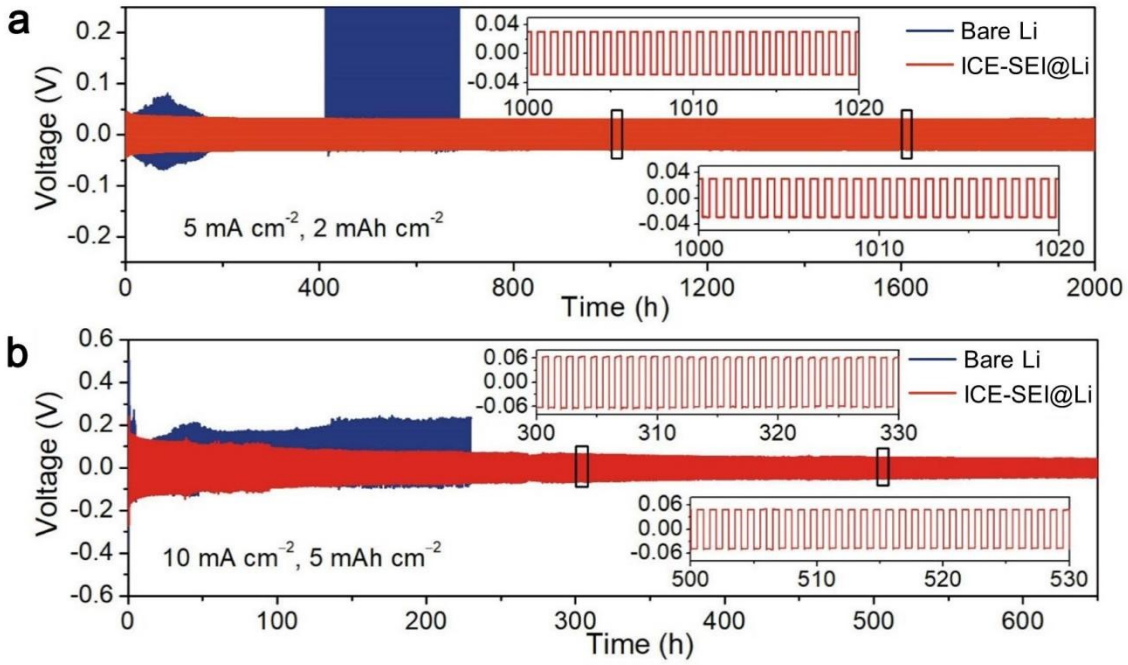

Fig. S36. Electrochemical performance of symmetric cells. a,b) Voltage-time profiles of symmetric cells with bare Li and ICE-SEI@Li at (a) 5 mA cm^{-2}, 2 mAh cm^{-2}, and (b) 10 mA cm^{-2}, 5 mAh cm^{-2}. Insets, corresponding enlarged voltage curves. Compared with the bare Li, symmetric cells with ICE-SEI@Li can ensure a more stable voltage plateau with lower voltage hysteresis.

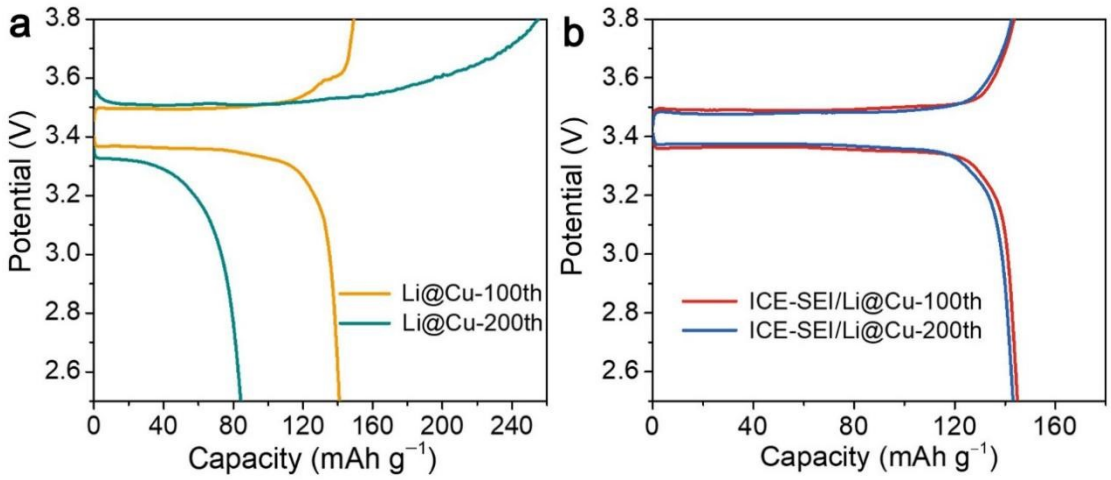

Fig. S37. The charge-discharge profiles of LFP full cells. a,b) The corresponding voltage profiles of LFP full cells with (a) bare Cu@Li and (b) ICE-SEI/Cu@Li at the 100th and 200th cycle. It exhibits that cell with ICE-SEI/Li@Cu can maintain lower overpotential than that of bare Li@Cu and better capacity retention after long-term cycling.

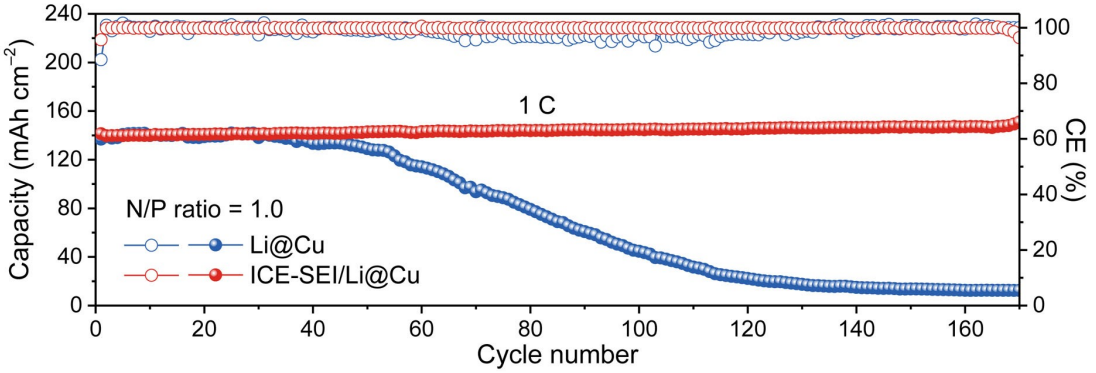

Figure S38. Cycling performance of full cell with bare Li@Cu and ICE-SEI/Li@Cu at 1 C with a high mass loading of LFP (3 mAh cm^{-2}) and limited Li of 3 mAh cm^{-2} (the N/P ratio is 1.0).

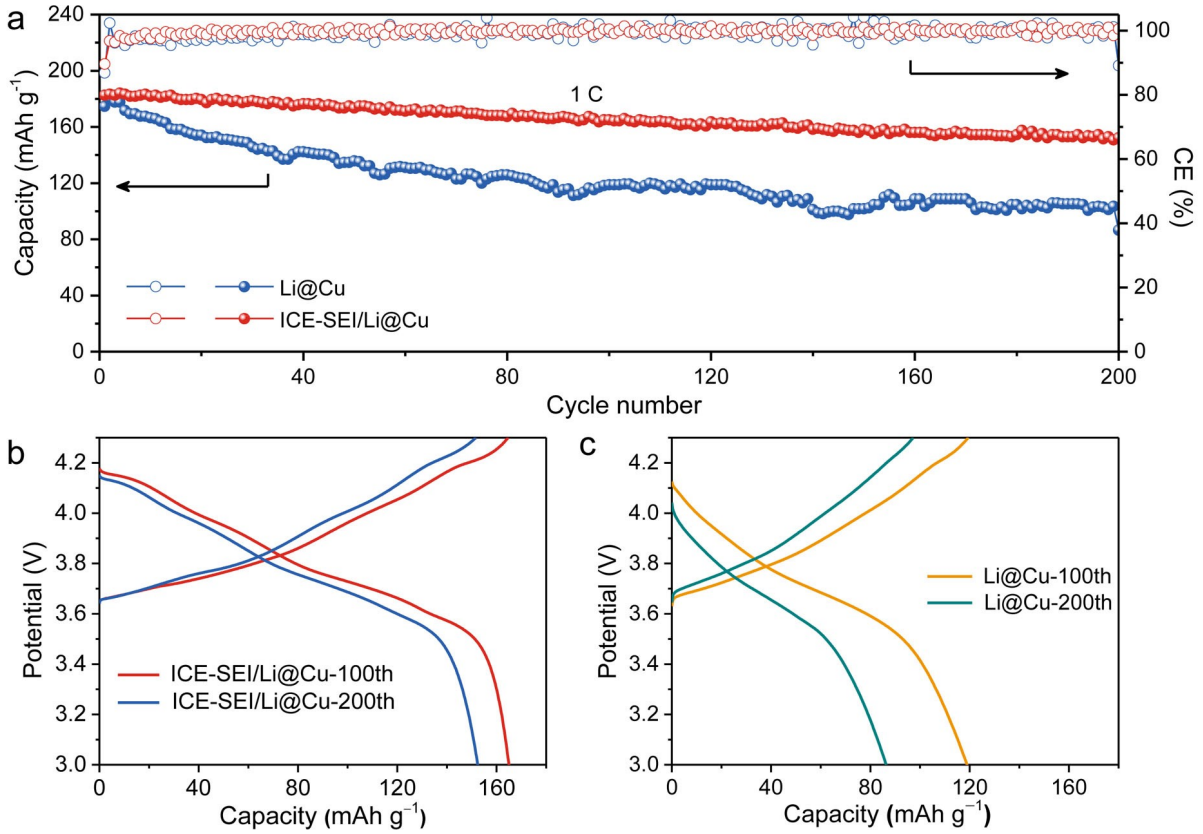

Figure S39. Electrochemical performance in the NCM811 full cells. a) Cycling performance of NCM811 full cells using bare Li@Cu and ICE-SEI/Li@Cu at 1 C. b,c) The corresponding voltage profiles of NCM811 full cells with (b) ICE-SEI/Li@Cu and (c) bare Li@Cu at the 100th and 200th cycle.

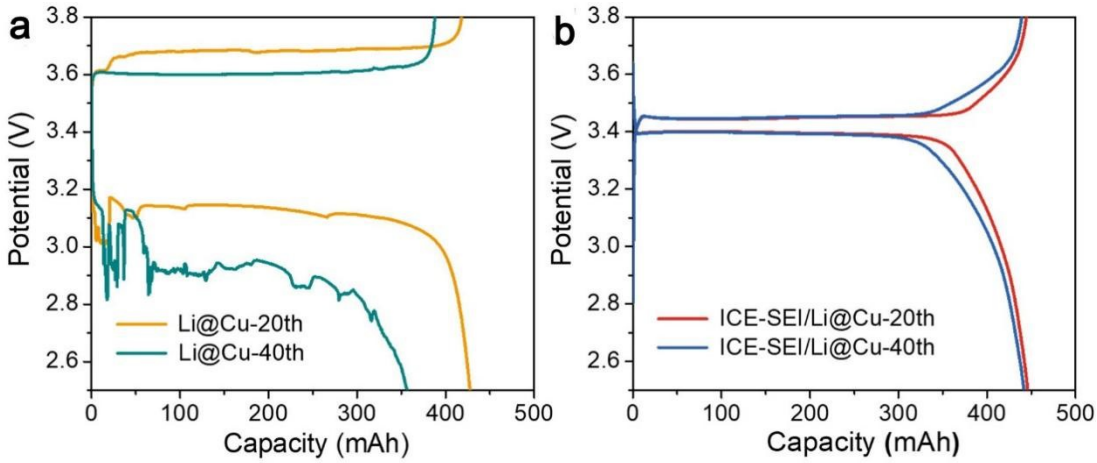

Fig. S40. The charge-discharge profiles of LFP pouch cells. a,b) The corresponding voltage profiles of LFP pouch cells with (a) bare Li@Cu and (b) ICE-SEI/Li@Cu at the 20th and 40th cycle. It shows that pouch cells with bare Li@Cu deliver a larger overpotential and the charge-discharge curve fluctuates up and down at the 40th cycle. By contrast, the overpotential of cells with ICE-SEI/Li@Cu is much smaller and it also can endow improved cycling stability in LFP pouch cells.

Supplemental Table

Table S1. The calculated bond dissociation energy for PAP molecule on Li (100) slab at different sites.

ΔG (eV)	①	②	③
Vacuum	2.57	3.80	4.12
Solvent (DOL: DME=1:1)	2.50	3.69	4.04
Vacuum-Li (100)	-4.41	-3.60	-1.47
Solvent (DOL: DME=1:1)-Li (100)	-3.99	-3.32	1.29

Supplemental Movies

Movie S1. ***In-situ*** **mechanical experiments of the ICE-SEI.** The ICE layer is generated as the polymer cavity due to the thermal effect of electron beam radiation on the ICE-SEI. The movie subsequently records the loading and unloading process in which the tungsten needle is employed to stab the polymer cavity.

Movie S2. ***In-situ*** **electrochemical experiments of the morphological evolution during Li plating with the ICE-SEI.** Initially, 1 mAh cm^{-2} of Li metal is deposited on the Cu grid and then 0.2 mAh cm^{-2} Li is stripped in the presence of the ICE-SEI. Subsequently, the movie records the process of *in-situ* Li plating in which a voltage of 5 V is applied between the two electrodes (Li spheres on Cu grid as the working electrode and Li metal on tungsten needle as a counter electrode) to drive the Li depositing.

Supplemental References

1. K. Wasanasuk, K. Tashiro, M. Hanesaka, T. Ohhara, K. Kurihara, R. Kuroki, T. Tamada, T. Ozeki, T. Kanamoto, *Macromolecules* 2011, **44**, 6441.
2. A. Jouhara, N. Dupre, A. C. Gaillot, D. Guyomard, F. Dolhem, P. Poizot, *Nat. Commun.* 2018, **9**, 4401.
3. T. Furukawa, H. Sato, R. Murakami, J. Zhang, I. Noda, S. Ochiai, Y. Ozaki, *Polymer* 2006, **47**, 3132.
4. N. W. Li, Y. Shi, Y. X. Yin, X. X. Zeng, J. Y. Li, C. J. Li, L. J. Wan, R. Wen, Y. G. Guo, *Angew. Chem. Int. Ed.* 2018, **57**, 1505.
5. M. Heller, U. S. Schubert, *e-Polymers* 2002, **2**, 27.
6. Y. Ma, L. Wei, Y. He, X. Yuan, Y. Su, Y. Gu, X. Li, X. Zhao, Y. Qin, Q. Mu, Y. Peng, Y. Sun and Z. Deng, Angew. Chem. Int. Ed., 2022, **134**, e202116291.
7. S. Xia, F. Li, X. Zhang, L. Luo, Y. Zhang, T. Yuan, Y. Pang, J. Yang, W. Liu, Z. Guo and S. Zheng, ACS Nano, 2023, **17**, 20689-20698.
8. C. Li, S. Liu, C. Shi, G. Liang, Z. Lu, R. Fu and D. Wu, Nat. Commun., 2019, **10**, 1363.
9. T. Liu, S. Chen, W. Sun, L. P. Lv, F. H. Du, H. Liu and Y. Wang, Adv. Funct. Mater., 2021, **31**, 2008514.
10. Y. Liu, Y. Wu, J. Zheng, Y. Wang, Z. Ju, G. Lu, O. Sheng, J. Nai, T. Liu, W. Zhang and X. Tao, Nano Energy, 2021, **82**, 105723.
11. G. Jiang, K. Li, F. Yu, X. Li, J. Mao, W. Jiang, F. Sun, B. Dai and Y. Li, Adv. Energy Mater., 2020, **11**, 2003496.
12. J. Yan, F. Liu, Z. Hu, J. Gao, W. Zhou, H. Huo, J. Zhou and L. Li, Nano Lett., 2020, **20**, 3798-3807.
13. G. Huang, P. Guo, J. Wang, S. Chen, J. Liang, R. Tao, S. Tang, X. Zhang, S. Cheng, Y.-C. Cao and S. Dai, Chem. Eng. J., 2020, **384**, 123313.
14. Y. Pang, M. Guan, Y. Pan, M. Tian, K. Huang, C. Jiang, A. Xiang, X. Wang, Y. Gong, Y. Xiang and X. Zhang, Small, 2022, **18**, 2104832.
15. W. Song, S. Cui, J. Zhang, S. Fan, L. Chen, H. M. Zhang, Y. Zhang and X. Meng, ACS Appl. Mater. Interfaces, 2023, **15**, 9421–9430.
16. X. Wang, S. Li, W. Zhang, D. Wang, Z. Shen, J. Zheng, H. L. Zhuang, Y. He and Y. Lu, Nano Energy, 2021, **89**, 106353.